경계형 모델을 사용한 초고강도 섬유보강 콘크리트거더의 파괴역학적 해석

Fracture Simulation of UHPFRC Girder with the Interface Type Model

궈 이 홍* 한 상 묵†
Guo Yi-Hong Han, Sang-Mook

요 지

본 연구는 선형 상보법으로 초고강도 섬유보강 콘크리트 I형보의 파괴역학적 해석을 수치해석으로 수행하였다. 기존의 보통강도 콘크리트에 대한 유사 취성 파괴역학적 수치해석을 기반으로 초고강도 섬유보강 콘크리트 재료역학적 구성모델 파괴 면에 인장경화 관계를 도입함으로써 초고강도 섬유보강 콘크리트 I형 거더 해석을 개선시켰다. 상수변형률 삼각형 요소에 꼭지점 또는 요소의 중앙점 절점을 배제하고 요소의 변에 절점을 배치한 결합된 삼각형 요소를 사용하였다. 인장영역에서는 경화/연화 파괴역학적 구성모델을, 전단영역에서는 연화 파괴역학적 구성모델을, 경계절점의 압축에 대해서는 연화 파괴역학적 구성모델을 사용하여 파괴역학적 해석을 수행하였다. Non-holonomic rate 형태로 경로에 의존적인 경화연화거동을 LCP로 방정식을 구성하였으며, 그 해는 PATH를 사용해서 구하였다. Piece-wise 비탄성 항복-파괴면은 두 개의 압축 caps, 두 개의 Mohr-Coulomb 파괴면, 인장항복면과 인장파괴면 등으로 구성하였다. 초고강도 섬유보강 콘크리트 거더의 변형거동과 파괴 상태와 비교하여 이 수치해석 방법에 대한 유효성을 검증하였다.

핵심용어 : 인장경화, 초고강도 섬유보강 콘크리트, 파괴역학, 선형 상보법

Abstract

This paper deals with the fracture simulation of UHPFRC girder with the interface type model. Based on the existing numerical simulation of quasi-brittle fracture in normal strength concrete, constitutive modeling for UHPFRC I-girder has been improved by including a tensile hardening at the failure surface. The finite element formulation is based on a triangular unit, constructed from constant strain triangles, with nodes along its sides and neither at the vertex nor the center of the unit. Fracture is simulated through a hardening/softening fracture constitutive law in tension, a softening fracture constitutive law in shear as well as in compression at the boundary nodes, with the material within the triangular unit remaining linear elastic. LCP is used to formulate the path-dependent hardening-softening behavior in non-holonomic rate form and a mathematical programming algorithm is employed to solve the LCP. The piece-wise linear inelastic yielding-failure/failure surface is modeled with two compressive caps, two Mohr-Coulomb failure surfaces, a tensile yielding surface and a tensile failure surface. The comparison between test results and numerical results indicates this method effectively simulates the deformation and failure of specimen.

Keywords *: tensile hardening, UHPFRC, fracture simulation, LCP*

1. 서 론

In the finite element analysis of concrete structure, two main models have been used for the numerical simulation of fracture: smeared-cracking model and discrete-cracking model. An overview of continuum damage-based approaches employed to research fracture in quasi-brittle materials is given by De(2002) who shows the smeared-cracking model can be cast into a damage format and can be conceived as

† 책임저자, 정회원 · 금오공과대학교 토목환경공학부 교수
Tel: 054-478-7614 ; Fax: 054-478-7629
E-mail: smhan@kumoh.ac.kr
* 금오공과대학교 토목환경공학부 토목공학과 박사과정

• 이 논문에 대한 토론을 2010년 4월 30일까지 본 학회에 보내주시면 2010년 6월호에 그 결과를 게재하겠습니다.

a special case of anisotropic damage models. A review of the abundant literature concerning discrete-cracking model has been given by Bolzon et al.(1994).

Many mathematical models have been used to formulate the fracture simulation, and linear complementarity problem(LCP) is one of them. LCP, a mathematical structure, consists of a linear equation which involves two orthogonal vectors with sign constrained components. The incremental formulation of LCP in rates deriving from a nonholonomic explanation of the discontinuity displacement locus, results in the stability and bifurcation criteria and the nonconventional solution displacement. LCP as a recurrent mathematical model governing both nonholonomic and holonomic analysis is an effective approach to simulation of fracture.

Investigations on LCP employed to formulate the fracture of material have been done. Bolzon et al.(1995) presented the holonomic and nonholonomic analysis of quasi-brittle fracture based on the cohesive-cracking idealization of quasi-brittle fracture processes with piecewise linear interface where LCP is used to formulate the discrete-cracking model, and a mathematical programming algorithms to seek the solutions. This approach can follow all possible equilibrium paths subject to the crack following the predefined crack, but there is generally no guarantee that all solution can be obtained in finite computation time and importantly, the crack profile has to be predefined. Tin-Loi et al.(2000) investigated the simulation of quasi-brittle fracture processes with the discrete-cracking model. In his investigations, the discrete-cracking model is also formulated as LCP, and the PATH solver is used to seek the solutions. The PATH solver is an implementation of a stabilized Newton method for the solution of LCP. The stabilization scheme employs a path-generation procedure which is used to construct a piecewise linear path from the current point to the Newton point; a step length acceptance criterion and a non-monotone path search are then used to choose the next iterate. The algorithm is remarkably efficient and reasonably robust, even for the nonlinear softening case. A detailed description on PATH solver has been given by Dirkes et al.(1995). Although one can usually assure this from the expected physical behavior of the structure, there is still no guarantee that all solutions for the given load level have been captured.

To avoid remeshing, Attard et al.(1999) proposed a discrete element that is a particle type model. Normally, it is assumed that the material in the particle is rigid or linear elastic and the hardening/softening effects are on the interface of particle. Based on the proposed discrete element, Attard et al.(2005) presented a piece-wise linear representation of "yield surfaces " which is used to approximate the inelastic failure surface. At the level of the interface nodes, the inelastic failure surface is a function of the normal and shear interface forces. Chaimoon(2007) developed the model proposed by Attard et al by including a compressive cap to simulate the unreinforced masonry walls under shear and compression. In these investigations(Attard et al., 2005; Chaimoon, 2007) the formulation attempts to simulate the quasi-brittle fracture without remeshing; and based on the solution of LCP, the results are obtained by using a mathematical procedure. The models proposed by Attard et al.(2005) and Chaimoon(2007) are fit for simulating normal-strength concrete, high-strength concrete and masonry, but not fit for ultra high performance fiber reinforced concrete(UHPFRC) because they do not consider the tensile hardening.

Although many numerical simulations of UHPFRC have been done, the material models in these simulations are plastic models and smear-cracking models(Giovanni et al., 2007; Kittinum et al., 2007; Chote et al., 2007; Han et al.,2009). In this paper, based on the investigations of F. Tin-Loi (2000, 2001, 2002) and Attard et al.(2005), an "interface" type model is developed to simulate UHPFRC I-girder. LCP is employed to formulate the proposed model, and the solutions are sought by a mathematical programming algorithm. Differing from all of the above mentioned models, this model considers the tensile hardening after cracking.

2. The Mechanical Properties of UHPFRC

The comparison of mechanical properties among normal concrete(NC), fiber reinforced concrete(FRC) and UHPFRC is listed in Table 1, in which it can be seen that UHPFRC has higher strength, stiffness and ductility due to its higher quantity of fiber reinforcement(usually 2% in volume of metallic fibers), as well as a denser and finer matrix. UHPFRC can be regarded as a linear-elastic, plastic-hardening, plastic-softening and crushing material in the compressive region, and a linear-elastic, crack-hardening and crack-softening material in the tensile region. UHPFRC has different fracture process from NC and FRC due to the tensile hardening after cracking.

As we know, the fracture process of NC includes three parts shown in Fig. 1. The first part is called linear-elastic zone in which there is no macro-crack and the material is regarded as linear-elasticity and isotropy; the second part is called fracture process zone or craze in which material behaves the softening; finally, material fails and loses the load carrying capacity when the cracking is full, and this part is called real crack zone. UHPFRC has the same behavior in the linear-elastic and real crack zone as NC, but it possesses different behavior in craze(shown in Fig. 2). After the linear-elastic behavior, micro-cracks develop into macro-cracks that are visible with the naked eye(ω=50μm)(Wu, 2008), and a reduction in stiffness is observed. Although macro- cracks occur, the tensile stress goes on increasing because the steel

Table 1 Comparison of mechanical properties among NC, FRC and UHPFRC

Property	Normal Concrete	Fiber Reinforced Concrete	UHPFRC
Compressive strength	21~27MPa	30~50MPa	50~400MPa
Bending strength	1~3MPa	5~15MPa	8~60MPa
E-modulus	21,000~ 35,000 MPa	30,000~ 40,000MPa	50,000MPa
Behavior Characteristics	Brittle	Quasi-Brittle	Ductile
Crack Characteristics	Partial	Partial+Multiple	Multiple

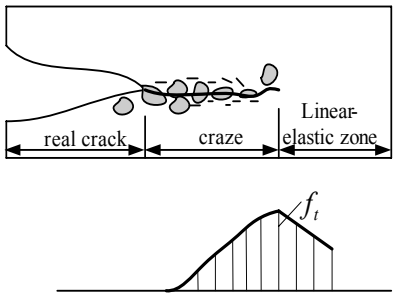

Fig. 1 Normal concrete fracture process

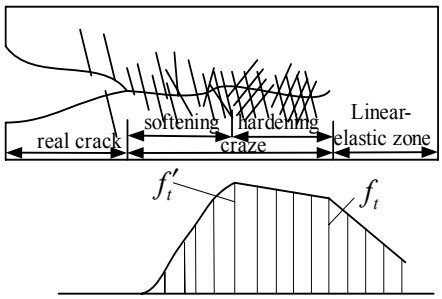

Fig. 2 UHPFRC fracture process

fiber has much higher strength and the fiber volume fraction is 2%. When the macro-crack saturation occurs and the crack width reaches a certain magnitude, the softening occurs. Hence, UHPFRC possesses hardening and softening behavior in fracture process zone. When no more stresses are transferred through the localized macro-crack, the real crack occurs. Based on the above formulation, two different constitutive relationships are employed to describe the tensile behavior of UHPFRC in linear-elastic zone and fracture process zone, respectively. In linear-elastic zone, the stress-strain relationship is used to describe the linear-elastic behavior; however, stress versus cracking width is applied to describing the hardening-softening behavior in fracture process zone. A more detailed theoretical model of multiple cracking failure mechanism is given by Wu et al. (2009).

3. The Finite Element

A discrete triangular unit formed by assembling nine constant strain triangles and condensing out the freedoms at the vertices(Attard, 2005) is used for the fracture simulation(shown in Fig. 3). As we know, the conventional finite element expresses the results as

stress-strain relationship; however this proposed element expresses the inelastic failure as a function of the normal and shear interface forces at the interface node so that it can effectively exhibit the failure state of interface node(tension, shear or compression) when the internal force reaches the yielding/failure surface shown in Fig. 5. Fracture is modeled through a hardening-softening fracture constitutive law in tension, a softening fracture constitutive law in shear as well as in compression at the boundary nodes along the sides of the triangular finite element, with the material within the triangular unit remaining linear elastic. Two nodes are distributed on each interface of the triangular(Fig. 4). Each node locates at $L_i/2n$ from the nearest vertex, where L_i is the length of interface and n a choice number(n equals 10 in this analysis). At each node, generalized interface displacements including outward normal and tangential displacement are defined. Corresponding to the generalized interface displacements at the interface nodes, the conjugate generalized forces are respectively the outward normal force Q_n and shear force Q_s shown in Fig. 4.

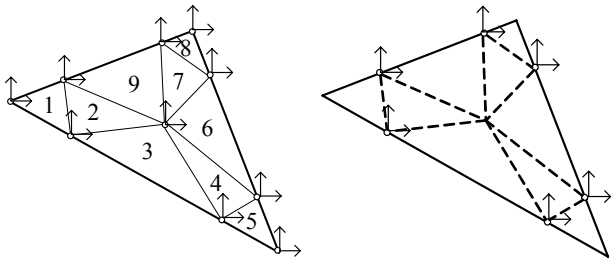

(a) Uncondensed triangle (b) condensed triangle

Fig. 3 Form of basic triangular element

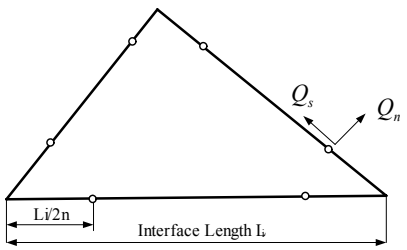

Fig. 4 Basic triangular unit

4 The Constitutive Model

4.1 The Piece-Wise Linear Inelastic Yielding-Failure/Failure Surface

At each of the interface nodes, the piece-wise linear failure surface developed by Maier(1970) is employed to describe the inelastic yielding-failure/failure surface which is a function of normal and shear interface forces. The piece-wise linear inelastic yielding-failure/failure surface shown in Fig. 5 consists of two compressive caps, two Mohr-coulomb failure surfaces, a tensile yielding surface and a tensile failure surface. In the investigations of Attard et al.(2005), a tensile cut-off is employed to describe the tensile failure because their investigative object is NC. However it has been mentioned that UHPFRC has different tensile behavior from NC and FRC, and the tensile hardening must be considered in the fracture process zone. Hence the piece-wise linear inelastic yielding-failure/failure surface in generalized force space has two surfaces employed to model the tensile behavior of UHPFRC: one is the yielding surface, and the other the failure surface. The piece-wise linear surface is named as the inelastic yielding-failure surface if it consists of the compressive caps, the Mohr-coulomb failure surfaces and the tensile yielding surface. The piece-wise linear surface is called the inelastic failure surface if it consists of the compressive caps, the Mohr-coulomb failure surfaces, and the tensile failure surface.

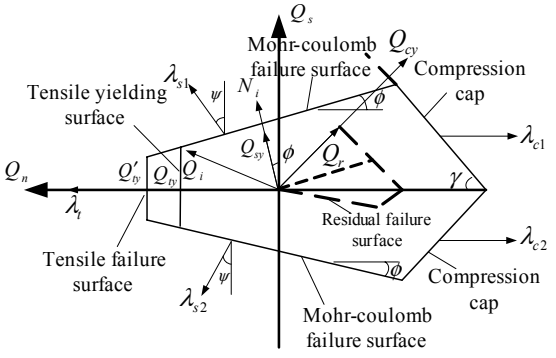

Fig. 5 Piece-wise linear inelastic yielding-failure/failure surface in generalized force space

For the nodal interface inelastic yielding-failure/failure surface, the interface multipliers(λ_t, λ_{s1}, λ_{s2}, λ_{c1} and λ_{c2}) are collected in the interface multipliers vector λ_i which are irreversible deformation vector (analogous to plastic multipliers used in plasticity):

$$\lambda_i = \{\lambda_t \quad \lambda_{s1} \quad \lambda_{s2} \quad \lambda_{c1} \quad \lambda_{c2}\}^T \tag{1}$$

where λ_t is the multiplier associated with the tensile yielding and failure surface; λ_{s1} and λ_{s2} are the multipliers associated with the Mohr-Coulomb failure surface; λ_{c1} and λ_{c2} are the multipliers associated with the compressive caps. In Fig. 5, Q_i is the resultant force vector at the interface node, Q_{ty} the tensile inelastic yielding force, Q'_{ty} the tensile inelastic failure force, Q_{sy} the shear inelastic failure force, Q_{cy} the compressive inelastic failure force and Q_r the residual compressive force. If the interface force is on the piece-wise linear inelastic yielding-failure surface, the initial inelastic yielding-failure vector r_{i1} is defined by

$$r_{i1} = \{Q_{ty} \quad Q_{sy} \quad Q_{sy} \quad Q_{cy} \quad Q_{cy}\}^T \tag{2}$$

If the interface force is on the piece-wise linear inelastic failure surface, the inelastic failure vector r_{i2} is given

$$r_{i2} = \{Q'_{ty} \quad Q_{sy} \quad Q_{sy} \quad Q_{cy} \quad Q_{cy}\}^T \tag{3}$$

If the force is on the residual failure surface, the residual force vector R_i is defined by

$$R_i = \{0 \quad 0 \quad 0 \quad Q_r \quad Q_r\}^T \tag{4}$$

The interface normality matrix N_i that contains the orientations of the normal to each yielding / failure plane and the dilatancy matrix V_i that defines the flow rule for the interface irreversible deformation multipliers are respectively expressed as

$$N_i = \begin{bmatrix} 0 & \cos\phi & -\cos\phi & \cos\gamma & -\cos\gamma \\ 1 & \sin\phi & \sin\phi & -\sin\gamma & -\sin\gamma \end{bmatrix} \tag{5}$$

$$V_i = \begin{bmatrix} 0 & \cos\psi & -\cos\psi & 0 & 0 \\ 1 & \sin\psi & \sin\psi & -1 & -1 \end{bmatrix} \tag{6}$$

where ϕ is the friction angle, and ψ the dilatancy angle. Q_{ty}, Q'_{ty}, Q_{sy}, Q_{cy} and Q_r are defined by

$$Q_{ty} = \frac{f_t L_i t_i}{2} \quad Q'_{ty} = \frac{f'_t L_i t_i}{2} \quad Q_{sy} = \frac{c\cos\phi L_i t_i}{2}$$
$$Q_{cy} = \frac{f'_c \sin\gamma L_i t_i}{2} \quad Q_r = \frac{f_r \sin\gamma L_i t_i}{2} \tag{7}$$

where f_t, f'_t, c, f'_c and f_r are the tensile yielding strength, the tensile ultimate strength, the cohesion, the compressive strength and the compressive residual, respectively; $\frac{L_i}{2}$ is half an interface length; t_i is the element thickness.

4.2 Hardening/Softening Law

The hardening/softening laws of UHPFRC for the interface forces at the interface nodes are shown in Fig. 6. A bilinear-branch hardening-softening curve is adopted for the tensile yielding and failure shown in Fig. 6(a), in which λ^h_{tc} represents the hardening crack opening width and λ_{tc} the critical crack opening width; the vertical paths represent either elastic loading or unloading. Along the hardening path or the softening path, the multiplier can only have positive increasing magnitude unless unloading occurs. After the critical crack opening displacement is exceeded, the crack opens or closes freely and the multiplier can increase or decrease in value. A single-branch softening curve shown Fig. 6(b) is assumed for the shear failure. λ_{sc} is the critical shear opening width. A single-branch softening curve shown in Fig. 6(c) is used for the compressive failure, in which λ_{cc} is the critical compressive opening width. The hardening/critical opening widths for tension are approximated by

$$\begin{cases} G_f^I = \frac{1}{2}\left[(f_t + f'_t)\lambda^h_{tc} + f'(\lambda_{tc} - \lambda^h_{tc})\right] \\ \lambda^h_{tc} = (0.4 \sim 0.5)\lambda_{tc} \end{cases} \tag{8}$$

where G_f^I is the mode I fracture energy. And the critical opening widths for shear and compression are estimated by the following equations(Chaimoon et al., 2007)

$$\lambda_{sc} = \frac{2G_f^{II}}{c\cos\psi} \qquad \lambda_{cc} = \frac{2G_f^{III}}{(f_c' - f_r)} \tag{9}$$

where G_f^{II}, G_f^{III} are the mode II and compressive fracture energy, respectively. The constitutive law of prestressing bar is considered as perfect elasticity-plasticity. The bond slip between the prestressing bar and the surrounding material is not considered implying the perfect bond between them.

An interface hardening/softening matrix H_i can indicate the evolution of the piece-wise linear inelastic yielding-failure/failure surface. If the multipliers are on the inelastic yielding-failure surface, matrix H_i is represented by H_{i1} and defined by

$$H_{i1} = \begin{bmatrix} \frac{(Q_{ty}' - Q_{ty})}{\lambda_{tc}^h} & \frac{(Q_{ty}' - Q_{ty})}{\lambda_{sc}}\beta & \frac{(Q_{ty}' - Q_{ty})}{\lambda_{sc}}\beta & 0 & 0 \\ -\frac{Q_{sy}}{\lambda_{tc}^h}\beta & -\frac{Q_{sy}}{\lambda_{sc}} & 0 & 0 & 0 \\ -\frac{Q_{sy}}{\lambda_{tc}^h}\beta & 0 & -\frac{Q_{sy}}{\lambda_{sc}} & 0 & 0 \\ 0 & 0 & 0 & -\frac{(Q_{cy} - Q_r)}{\lambda_{cc}} & 0 \\ 0 & 0 & 0 & 0 & -\frac{(Q_{cy} - Q_r)}{\lambda_{cc}} \end{bmatrix} \tag{10}$$

If the multipliers are on the inelastic failure surface, matrix H_i is represented by H_{i2} and defined by

$$H_{i2} = \begin{bmatrix} -\frac{Q_{ty}'}{(\lambda_{tc} - \lambda_{tc}^h)} & -\frac{Q_{ty}'}{\lambda_{sc}}\beta & -\frac{Q_{ty}'}{\lambda_{sc}}\beta & 0 & 0 \\ -\frac{Q_{sy}}{(\lambda_{tc} - \lambda_{tc}^h)}\beta & -\frac{Q_{sy}}{\lambda_{sc}} & 0 & 0 & 0 \\ -\frac{Q_{sy}}{(\lambda_{tc} - \lambda_{tc}^h)}\beta & 0 & -\frac{Q_{sy}}{\lambda_{sc}} & 0 & 0 \\ 0 & 0 & 0 & -\frac{(Q_{cy} - Q_r)}{\lambda_{cc}} & 0 \\ 0 & 0 & 0 & 0 & -\frac{(Q_{cy} - Q_r)}{\lambda_{cc}} \end{bmatrix} \tag{11}$$

The off-diagonal terms in the matrix H_{i1} and H_{i2} represent interaction between the interface tensile force and the interface shear force. β is an interaction parameter. The piece-wise linear inelastic yielding-failure/failure surface contracts in an isotropic manner if β equals to unity. It is assumed that no interaction between the shear and compression failure planes in this paper.

The evolution of the interface inelastic yielding-failure/failure surface is represented by the vector ξ_i

$$\xi_i = r_i + H_i\lambda_i \tag{12}$$

If the interface force is on the piece-wise linear

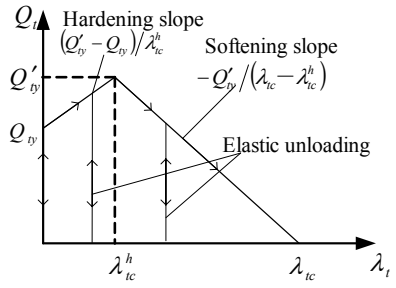

(a) Constitutive law for tensile mode

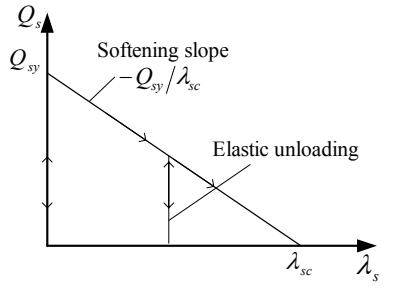

(b) Constitutive law for shear mode

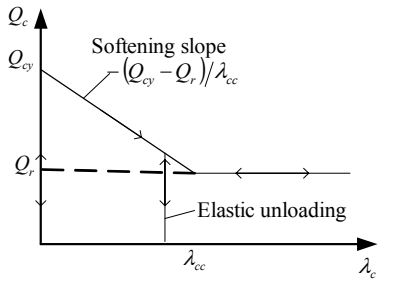

(c) Constitutive law for compressive mode

Fig. 6 Interface constitutive law of UHPFRC

inelastic yielding-failure surface, r_i and H_i are respectively defined by r_{i1} and H_{i1}. The evolution of the interface inelastic yielding-failure surface is expressed as

$$\xi_i = r_{i1} + H_{i1}\lambda_i \tag{13}$$

If the interface force is on the piece-wise linear inelastic failure surface, r_i and H_i are respectively defined by r_{i2} and H_{i2}. The evolution of the interface inelastic failure surface is expressed as

$$\xi_i = r_{i2} + H_{i2}\lambda_i \tag{14}$$

4.3 Structural Governing Equations

For a complete structure, the material behavior can be described by the structure generalized displacements q and the structure generalized forces Q:

$$Q = Sq \tag{15}$$

The structure generalized displacements are the sum of recoverable elastic component q_e and irreversible inelastic component q_p. Therefore,

$$q = q_e + q_p \tag{16}$$

If it is assumed that there is no damage(degrading of the instantaneous unloading stiffness) through the history of loading and that the instantaneous unloading stiffness is equal to the initial secant stiffness, Q can be expressed in terms of the elastic component q_e of the structure generalized displacement as

$$Q = Sq_e \tag{17}$$

The relationships defined in Eq.16 and Eq.17 are diagrammed in Fig. 7. For an associated flow rule, the inelastic component q_p are given

$$q_p = N\lambda \tag{18}$$

for a non-associated flow rule, q_p are given

$$q_p = V\lambda \tag{19}$$

where N is the structure normality matrix that collects the interface normality matrices, and V is the structure dilatancy matrix that collects the interface dilatancy matrices. According to the relation between global coordinate and generalized coordinate, the basic relations are given:

$$\begin{aligned}
&F = AQ \quad A^T u = q \quad Q = Sq_e \quad q_e = A^T u - V\lambda \\
&F = AQ = ASq_e = ASA^T u - ASV\lambda = Ku - ASV\lambda \\
&u = K^{-1}F + K^{-1}ASV\lambda = \alpha K^{-1}F^{\text{unit}} + D\lambda = u_e + u_p \\
&Q = \alpha SA^T K^{-1}F^{\text{unit}} + \left(SA^T K^{-1}AS - S\right)V\lambda = \alpha Q_e^{\text{unit}} + ZV\lambda = Q_e + Q_p
\end{aligned} \tag{20}$$

where F is the structure global force vector, A the assembled structure equilibrium matrix, u the structure global displacement vector, K the structure stiffness matrix, α a scalar load factor; F^{unit} the structure global load vector due to a unit load factor. u_e and u_p are respectively the elastic and inelastic components of u. Q_e^{unit} is the elastic component of Q due to a unit load factor. Q_e and Q_p are respectively the elastic and inelastic component of Q

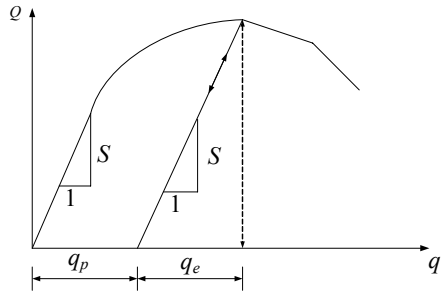

Fig. 7 relation between interface forces and displacements

If the generalized force vector reaches the inelastic yielding-failure/failure surface, the inelastic yielding-failure/failure is activated. The projection of Q in all phases must satisfy the following condition.

$$\varphi = N^T Q - r - H\lambda \le 0 \tag{21}$$

By substituting Q_e and Q_p in Eq.20 into Eq.21, we can obtain

$$\begin{aligned}\varphi &= \alpha N^T Q_e^{\text{unit}} - r + \left(N^T Z V - H\right)\lambda \le 0 \\ &= \alpha N^T Q_e^{\text{unit}} - r + W\lambda \le 0\end{aligned} \tag{22}$$

Eq.22 is in holonomic form and can be written in nonholonomic rate form as

$$\dot{\varphi} = \dot{\alpha} N^T Q_e^{\text{unit}} + W\dot{\lambda} \le 0 \tag{23}$$

where φ is a potential function vector, H is the structure hardening/softening matrix which assembles the interface hardening/softening matrix. It is noticeable that the tensile interface forces at the nodes are on the piece-wise linear inelastic yielding-failure surface or on the piece-wise linear inelastic failure surface when assembling the structure hardening/softening matrix. At first, the structure hardening/softening matrix consists of H_{i1} because the generalized forces should firstly reach the piece-wise linear inelastic yielding-failure surface. When the generalized force at the ith interface node reaches the piece-wise linear inelastic failure surface, the corresponding ith node H_{i1} should be changed into H_{i2} in the structure hardening/softening matrix H. Eq.23 is a standard LCP, which satisfies the following constraints:

$$\dot{\lambda} \ge 0 \qquad \dot{\varphi}\dot{\lambda} = 0 \tag{24}$$

Based on the original procedure, programs concerning the proposed constitutive law and corresponding pre- and post-processing are made. In the formulation of LCP, the hardening/softening behavior after linear elasticity can be effectively simulated. The flow chart of solution algorithm is given in Fig. 8

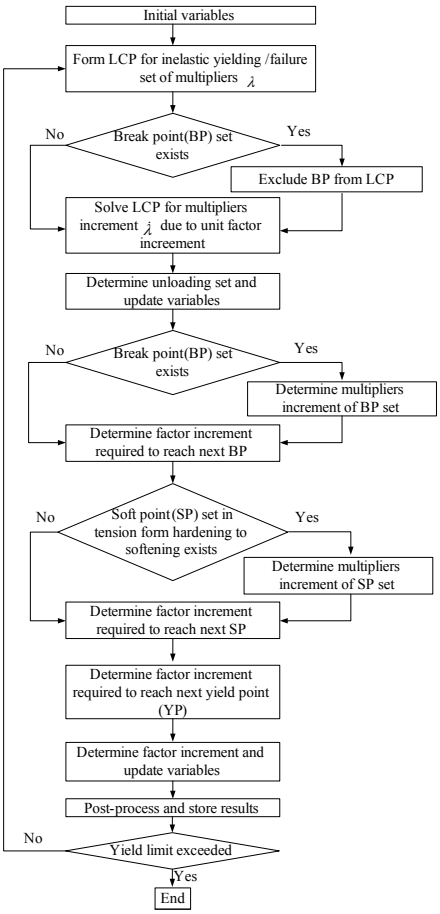

Fig. 8 The flow chart of solution algorithm

5. Simulation of UHPFRC I-Girder

5.1 Description of Specimen

Three three-point bending girders that have been tested are presented. Specimen 1 and specimen 2 have the same section and geometrical dimension shown in Fig. 9. The difference between the two specimens is specimen 1 without prestressing force and specimen 2 with pre-tension. The magnitude of pre-tensioning force is 80% of the yielding stress. The section and geometrical dimension of specimen 3 is shown in Fig. 10. The magnitude of post-tensioning force is also 80% of the yielding stress. The declining edges of the upper and lower flange simplified to be straight edges are respectively shown in Fig. 11 for specimen1and

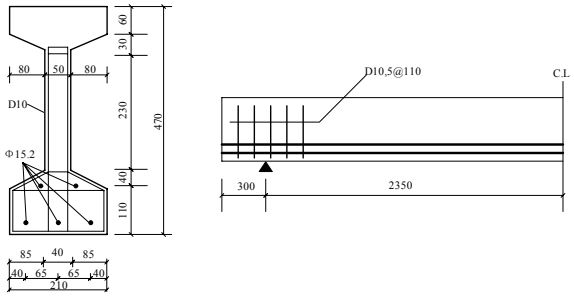

Fig. 9 Section and geometrical dimension of specimen 1 and specimen 2

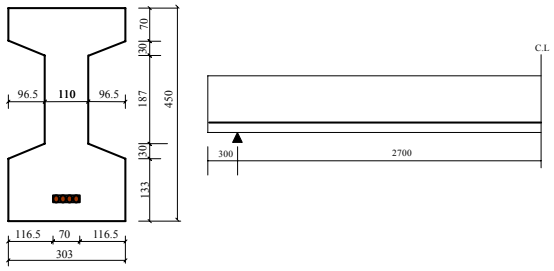

Fig. 10 Section and geometrical dimension of specimen 3

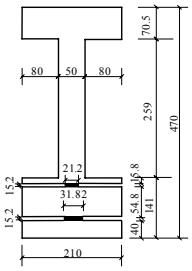

Fig. 11 Simplified section of specimen 1 and specimen2

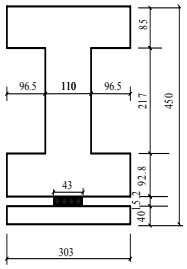

Fig. 12 Simplified section of specimen 3

specimen 2, and in Fig. 12 for specimen3. It is noted that the prestressing bar is regarded as a layer in which the UHPFRC part is ignored because this 2D model cannot consider two kinds of material properties in the same layer. The meshing of specimen 1 and specimen 2 is shown in Fig. 13 and the meshing of specimen 3 shown in Fig. 14.

The material parameters to be input are listed in Table 2 when the model is defined. There is no research on the friction angle of UHPFRC until now, so a friction angle 37° is assumed according to the friction angle of high strength concrete here. The dilatancy angle defines the flow direction for the interface irreversible deformation multipliers. The dilatancy angle equals to the friction angle because the associated flow rule is used in this paper. The critical opening widths are decided by the fracture energy using Eq.8 and Eq.9. A 2% fiber volume fraction is used because the material cannot show

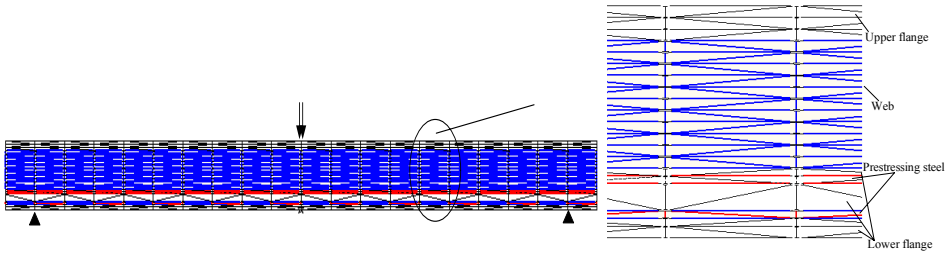

Fig. 13 Meshing of specimen 1 and specimen 2

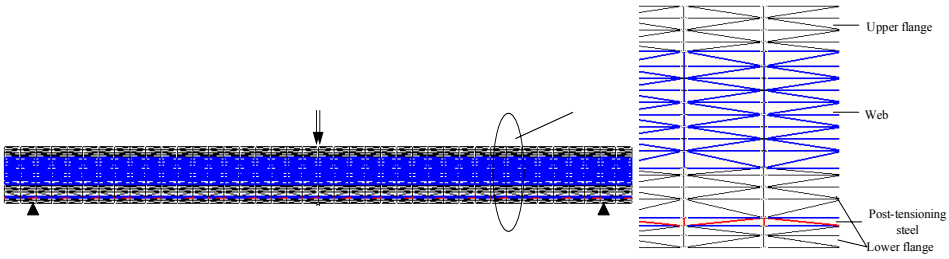

Fig. 14 Meshing of specimen 3

Table 2 material parameters

	Specimen1	Specimen2	Specimen3	All the specimens
	UHPFRC			Prestressing bar
Young's Modulus(GPa)	42	45	35	186
yielding tensile strength(MPa)	6	8	6	1000
ultimate tensile strength(MPa)	10	12	8	——
compressive strength(MPa)	150	150	140	1000
friction angle(°)	37	37	37	0
dilatancy angle(°)	37	37	37	0
hardening crack opening width(mm)	0.8	0.8	0.6	∞
critical crack opening width(mm)	1.7	1.7	1.5	——
critical shear opening width(mm)	1	1	1	∞
critical compressive opening width(mm)	1.5	1.5	1.5	∞

apparent ductility if the volume fraction of fiber is lower than 2%, and the influence of fiber on the tensile behavior and ductility is small when the volume fraction of fiber is beyond 2%.

5.2 Comparison of Load-Deflection Relationship

The comparison of load-deflection relationship between the test results and the numerical results with LCP are shown in Fig. 15~Fig. 17, where the solid line represents the results of test and the line with triangular the results of numerical simulation. It can be seen from the comparison of specimen1 shown in Fig. 15 that the two responses are in good agreement with each other in the elastic zone and the forpart of plastic zone, and the discrepancy of deflection is relative big near the peak load. Two reasons lead to the difference: one is the uncertainty of material inelastic properties, and the other is the experimental error of small specimen test. During testing small specimen to decide the material parameters, the fracture energy may be estimated larger than the real magnitude, which means the numerical model with the estimated fracture energy has relative big deflection. More exactly describing the inelastic properties of material and reducing the experimental error of small specimen are the methods to improve the numerical result. The numerical peak load is only 0.7% greater than the experimental value, so this model effectively predicts the ultimate load.

The comparison of specimen 2 shown in Fig. 16 indicates a good matching. In this comparison, this

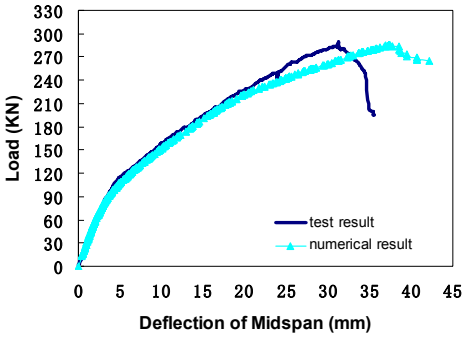

Fig. 15 The load-deflection curve comparison of specimen 1

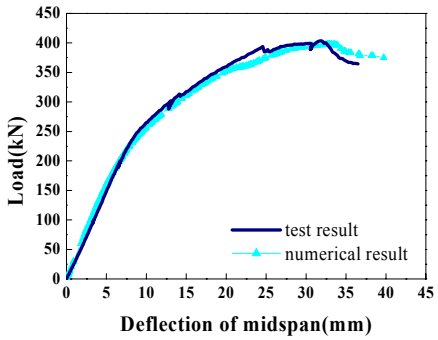

Fig. 16 The load-deflection curve comparison of specimen 2

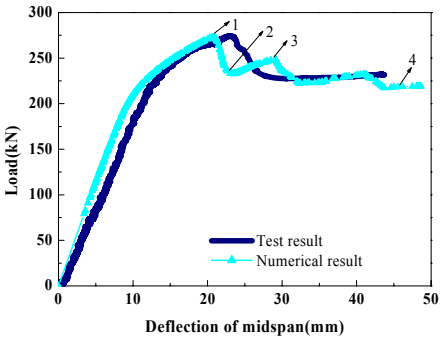

Fig. 17 The load-deflection curve comparison of specimen 3

model exactly evaluates the load and corresponding displacement in different region. The largest gap of load between the two curves is 8kN(the numerical load and the experimental load are respectively 385kN and 393kN) when the deflection is 24.18mm, and the difference is controlled within 2%. This comparison further indicates the reliability of this model.

Fig. 17 shows the two curves agree with each other before the peak load, and the difference is under 2%, but the discrepancy is relative big after peak load. The numerical curve exhibits apparent unloading and reloading after the first peak load, which did not happen in the test. Although the discrepancy also caused by the uncertainty of material inelastic properties exists, the two responses have the similar tendency that means this model can effectively capture the girder behavior before and after peak load.

5.3 Numerical Simulation of Failure Mode and Discussion

In this subsection, only the failure mode of specimen 3 is presented. As shown in Fig. 17, this numerical simulation exists unloading and reloading

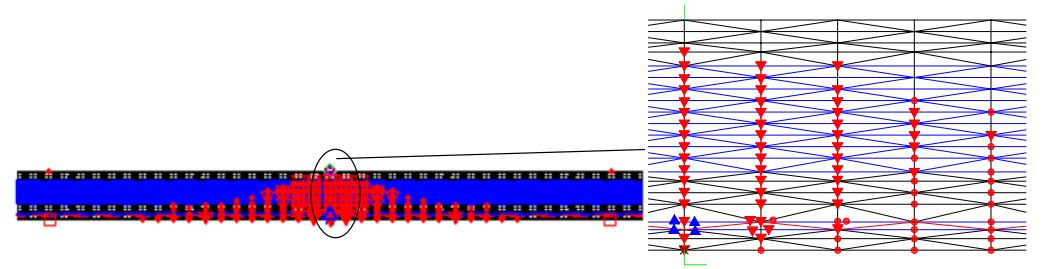

(a) Failure nodes of point 1

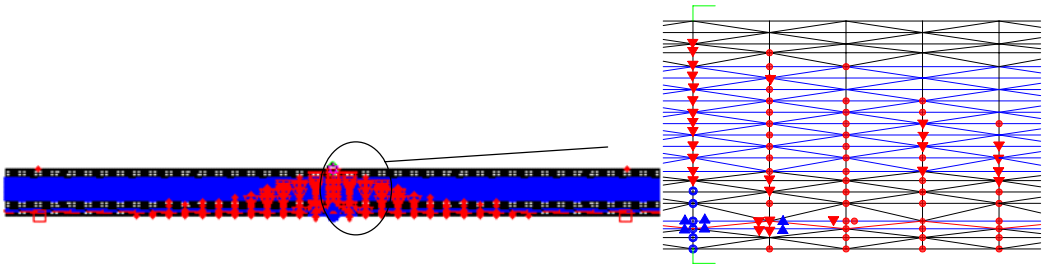

(b) Failure nodes of point 2

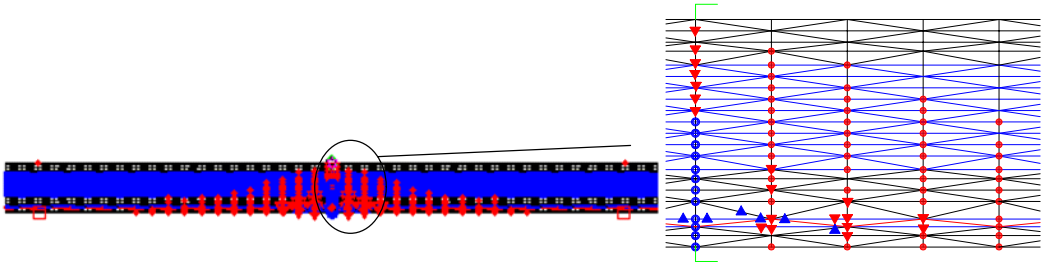

(c) Failure nodes of point 3

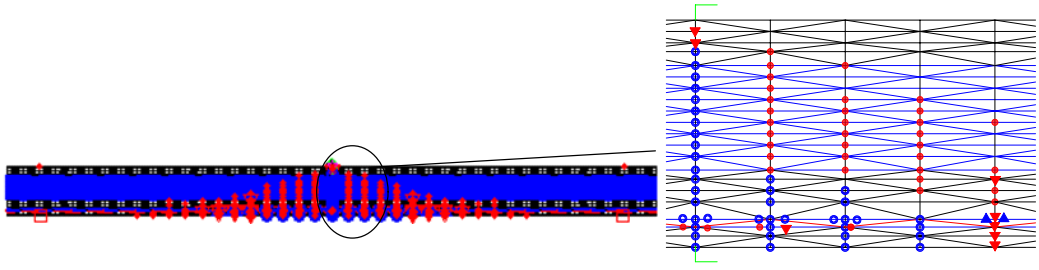

(d) Failure nodes of point 4

(o: critical displacement ▼:tensile hardening/softening ▲:shear softening ■: compression softening·:Unloading)

Fig. 18 Failure process of specimen3 after peak load

after the peak load. Hence, to be able to get a better understanding of the failure behavior of UHPFRC I-girder and how cracks propagate, several points along the load-deflection path are observed in detail. The considered points shown in Fig. 17 are 1, 2, 3, 4 on the load-deflection curve, and the corresponding failure nodes are shown in Fig. 18(a,b,c,d). In Fig. 18(a), unloading of some nodes occurs and no node reaches the critical crack opening displacement. The node at the bottom midspan is the first to reach the critical crack opening displacement after the peak load, and then the tensile crack propagates from the bottom midspan to the load point that can be found in Fig. 18(b,c). The tensile crack propagates sharply after the point 3, and the crack propagates not only along the section of midspan, but also both sides of midspan. Finally, the girder completely loses the load carrying capacity shown in Fig. 18(d). The inelastic failure during the simulation is mainly on the tensile inelastic yielding/failure surface indicating that the failure is predominately controlled by the flexural failure that is in agreement with the test result. The states of peak load and failure in the test are shown in Fig. 19 and Fig. 20, respectively. By comparison, it can be seen that the model simulates the failure process well.

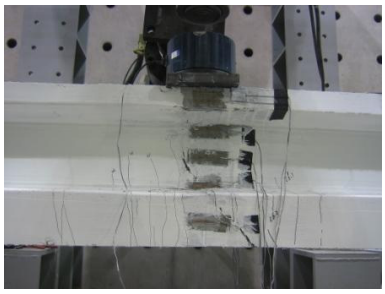

Fig. 19 The state of peak load

Fig. 20 The state of failure

5.4 Comparison with Diana Results

The proposed model is a new method for the fracture simulation of UHPFRC. To further verify the effectivity of this model, a comparison with Diana results is presented in this section. The material model offered in Diana is an elastic-plastic fracture model which considers the strain hardening after crack in tension and adopts the Drucker-Prager criterion in compression. The difference between the two models is that the model in Diana is a smear-

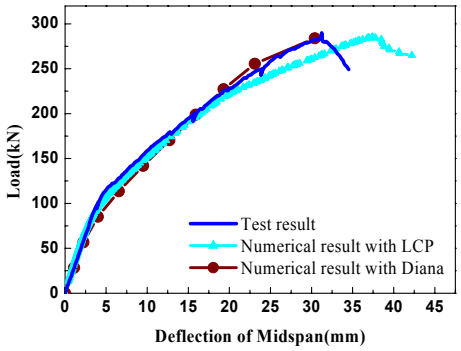

Fig. 21 The load-deflection curve comparison of specimen1with Diana

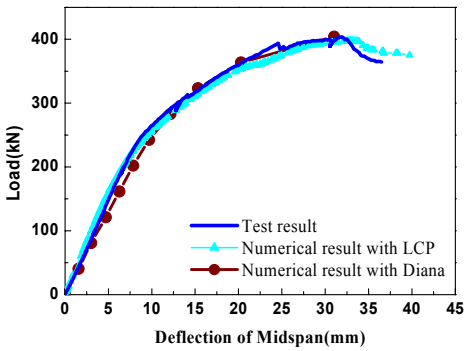

Fig. 22 The load-deflection curve comparison of specimen2 with Diana

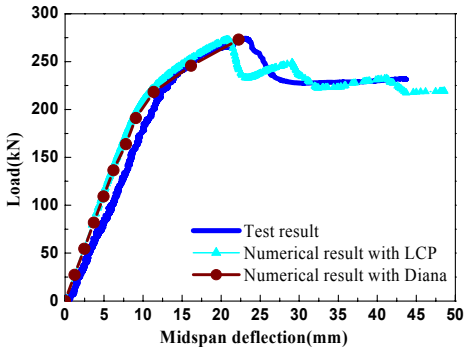

Fig. 23 The load-deflection curve comparison of specimen3 with Diana

cracking model and the stress-cracking strain relationship for the description of tensile behavior; however the proposed model is an "interface" type model and the interface force-cracking width relationship for the formulation of tensile constitutive law. The strength and Young's modulus needed inputting when defining the model in Diana is listed in Table 2. The comparisons are shown in Fig. 21~Fig. 23. Fig. 22 and Fig. 23 show the comparison of numerical result between LCP and Diana are in good agreement with each other. The difference of deflection near the peak load in Fig. 21 is mainly caused by the experimental error of small specimen that has been explained in section 5.2

6. Conclusions

Based on the existing numerical simulation of quasi-brittle fracture in normal strength concrete, a model is developed to simulate the fracture of UHPFRC girder. The piece-wise linear inelastic yielding-failure/failure surface is modeled with two compressive caps, two Mohr-Coulomb failure surfaces, a tensile yielding surface and a tensile failure surface.

The developed model formulated by LCP can effectively simulate the fracture of UHPFRC. The tensile hardening in fracture process zone must be considered for the fracture simulation of UHPFRC. The piece-wise linear inelastic yielding-failure/failure surface is fit for the fracture simulation of UHPFRC.

By the comparison between the test results and the numerical results with the interface type model, the proposed model fits to simulate the load-deflection relationship, the cracking characteristics and the failure process for UHPFRC, and the discrepancy of peak load is controlled within 2%. The agreement of the two numerical results between the interface type model and Diana further indicates the effectivity of the proposed model.

The proposed model can directly exhibit the failure state of interface node(tension, shear or compression) under different load level.

Acknowledgments

This paper was supported by Research Fund, Kumoh National Institute of Technology.

Reference

Attard, M.M., Tin-Loi F. (1999) Fracture Simulation Using a Discrete Triangular Element, ACMSM 16 Sedney, NSW, Austrilia, pp.11~16.

Attard, M.M., Tin-Loi, F. (2005) Numerical Simulation of Quasi-Brittle Fracture in Concrete, *Engineering Fracture Mechanics*, 72, pp.387~411.

Bolzon, G., Mairer, G., Novati, G. (1994) Some Aspects of Quasi-Brittle Fracture Analysis as a Linear Complementarity Problem, *Fracture & Damage in Quasi-Brittle Structure*, pp.159~174.

Bolzon, G., Mairer, G., Tin-Loi, F. (1995) Holonomic and Nonholonomic Simulations of Quasi-Brittle Fracture: A Comparative Study of Mathematical Programming an Approach, *Fracture Mechanics of Concrete Structures*, 2, pp.885~898.

Chaimoon, K. (2007) Numerical Simulation of Fracture in Unreinforced Masonry, Ph.D thesis.

Chaimoon, K., Attard, M.M. (2007) Modeling of Unreinforced Masonry Wall under Shear and Compression, *Engineering structures*, 29, pp.2056~2068.

Chote, S., Barzin, M. (2007) Flexural Modeling of Strain Softening and Strain Hardening Fiber Reinforced Concrete, *5th High Performance Fiber Reinforced Cement Composites(HPFRCC5)*, pp.155~164.

De, B.R. (2002) Fracture in Quasi-Brittle Materials: A Review of Continuum Damage-Based Approaches, *Engineering Fracture Mechanics*, 69, pp.95~112.

Dirkes, S.P., Ferris, M.C. (1995) The Path Solver: a Nonmonotone Stabilization Scheme for Mixed Complementarity Problems, *Optim. Meht. Software*, pp.123~156.

Giovanni, M., Alberto, M. (2007) Strengthening of R/Cbeams with High Performance Fiber Reinforced Cementituious Composites, *5th High Performance Fiber Reinforced Cement Composites*, pp.389~397.

Han, S.M., Guo, Y.H. (2009) Nonlinear Finite Element Analysis of UHPFRC I-Beam on the Basic

of an Elastic-Plastic Fracture Model, 한국전산구조공학회논문집, 22(3), pp.199~209.

Kittinum, S., Sherif E.T. (2007) Three-Dimensional Plasticity Model for High Performance Fiber Reinforced Cement Composites, *5th High Performance Fiber Reinforced Cement Composites(HPFRCC5)*, pp.231~240.

Maier, G. (1970) A Matrix Structural Theory of Piecewise-Linear Elastoplsticity with Interaction Yield Planes, *Meccanica*, 5, pp.54~66.

Que, N.S., Tin-Loi, F. (2002) Numerical Evaluation of Cohesive Fracture Parameters from a Wedge Splitting Test, *Engineering Fracture Mechanics*, 69, pp.1269~1286.

Tin-Loi, F., Li, H. (2000) Numerical Simulations of Quasi-Brittle Fracture Processes Using the Discrete Cohesive Crack Model, *Mechanical Sciences*, 42, pp.367~379.

Tin-Loi, F., Xia, S.H. (2001) Holonomic Softening: Models and Analysis, *Sruct. & Mech.*, 29, pp.65~84.

Wu, X.G. (2008) Flexure and Shear Behavior of Ultra High Performance Concrete Post Tension I Shaped Composite Girder, Ph.D thesis.

Wu, X.G., Han, S.M. (2009) Multiple Cracking Model of Fiber Reinforced High Performance Cementitious Composites under Uniaxial Tension, *Concrete Structures and Material*, 3(1), pp.71~77.

● 논문접수일 2009년 9월29일
● 논문심사일
1차 2009년10월13일
2차 2009년11월16일
● 게재확정일 2009년11월27일